Supplemental Information: Turn all the lights off: Bright and dark field second harmonic microscopy to select contrast mechanisms for ferroelectric domain walls

Peter Hegarty,[1] Henrik Beccard,[1] Lukas M. Eng,[1,2] and Michael Rüsing[1]

[1)]*TU Dresden, Institute of Applied Physics, Nöthnitzer Strasse 61, 01187 Dresden, Germany*

[2)]*ct.qmat: Dresden-Würzburg Cluster of Excellence—EXC 2147, TU Dresden, 01062 Dresden, Germany*

(*Electronic mail: Correspondence: peter_andrew.hegarty@tu-dresden.de)

(Dated: 24 May 2022)

S1. OBTAINING SIGNAL PROFILES

The .czi files that contain the recorded line scans for each parameter configuration are loaded into ImageJ, where each single one-dimensional line can be plotted on its own. However, as this makes a larger-scale comparison along the depth of a sample tedious, it is far more useful to generate an orthogonally projected image from the gathered line scans. This process is depicted schematically in Fig. S1. The collected line scans are read while the metadata of the .czi file is taken to generate a framework with the total dimensions of the scanning image, both laterally and axially. Each line scan is then converted to a single pixle-wide strip of grayscale and inserted into the framework at the corresponding axial position. The result is a 2D-slice of the sample cut perpendicular to the domain walls (DWs), showing the signal behavior at various depths at a glance.

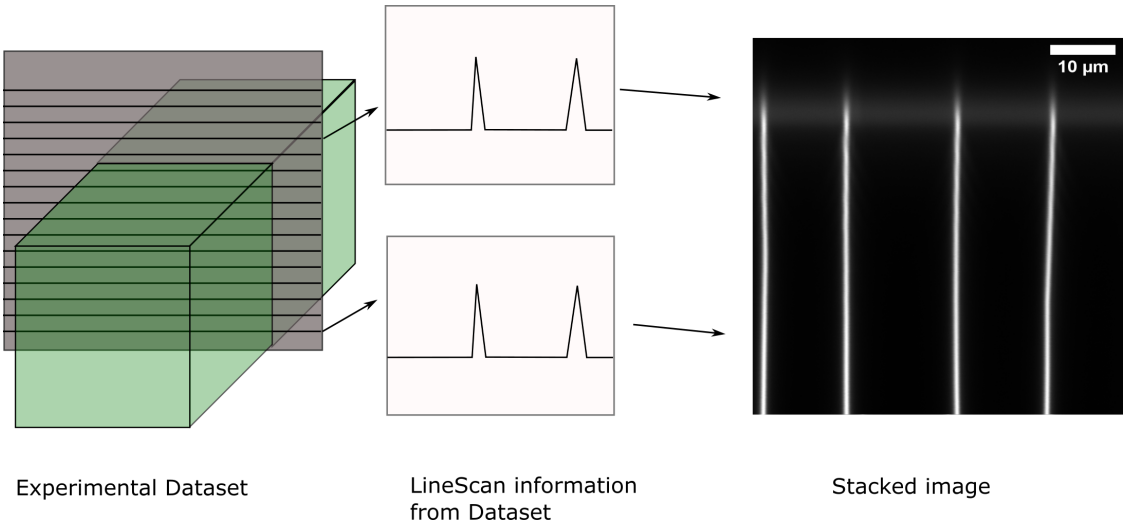

FIG. S1. Schematic flow-diagram of the process by which the 2D image of the sample is generated. The collected 1D line scans (a) are converted into a grayscale strip (b) and stacked vertically to create the 2D slice image (c).

The scan images shown in Fig. 4 (main text) display exactly such orthogonal projections, and are the basis later used to extract the horizontal profile at the correct depth for each sample and parameter configuration.

The process and the line profiles required to perform it is shown sequentially in Fig. S2, and consists of a number of individual steps. The initial step is to first locate the depth or vertical

position at which the surface is located. To do this, the image profile is read along the vertical axis (red line (1.) in Fig. S2). This will be the position of maximum signal when scanning vertically into the domain region. The domain walls are to be avoided as they appear far brighter than the surrounding domain, thereby making an exact location of the surface difficult. Once the surface is allocated, it is then used to determine the exact absolute position in the image that corresponds to a desired optical depth.

In the case of an overexposure (and therefore the formation of an extended plateau showing the

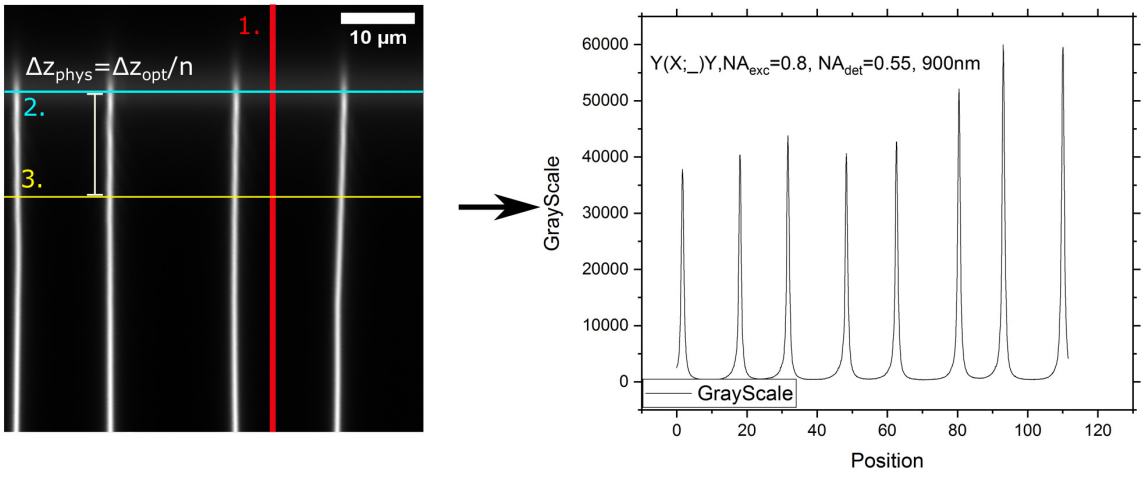

FIG. S2. Step-by-step process by which the correct horizontal profiles are read out from the orthogonal projection. Subfigure (a) shows a sample orthogonal image. The extraction steps are indicated by colored lines and a corresponding number in image (a). 1.) The signal profile is extracted vertically within the crystal, avoiding the domain walls. 2.) The depth at which the extracted vertical profile is at its maximum is calculated and allocated as the surface position. 3.) The horizontal profile is extracted at the chosen depth below the surface as calculated by $\Delta z_{phys} = \frac{\Delta z_{opt}}{n}$. Subfigure (b) shows the resulting profile.

maximum signal) the plateau is assumed to be symmetric around the surface and the median position within is taken as the surface position.

The optical path length of a beam is proportional to the refractive index of the medium it is propagating in, meaning that while physically two sets of two points may be the same distance apart in different media, a light beam will experience an altered path length. Examples for these effects are discussed in work done by Hell et al.[1] The problem this causes for the images that have been compiled, is that the axial or vertical position is given by the "mechanical" position of the posi-

tioning stage. As such, while it is immediately possible to start at the located surface and read the profile at the line 50 μm below it, this will not correspond to an optical depth of 50 μm, instead being closer to approximately 100 μm (for an $n = 2$ medium). A basic way to at least partially correct for this effect is to calculate the necessary physical depth by dividing the desired optical depth by the medium's refractive index as annotated in Fig. S6:

$$\Delta z_{phys} = \frac{\Delta z_{opt}}{n}. \tag{1}$$

This corrected vertical position is subsequently used to acquire the correct line profile, which is saved as a .csv-file.

S2. EMISSION CHARACTERISTICS AT DOMAIN WALLS

In the present work, we compare the DW signal to the domain signal emitted at the surface to verify that there must be an additional effect present causing the observed behavior. In order to evaluate the behavior of our detected SHG signal with respect to an identification as CSHG, we require a base expectation for SHG emission which does not involve CSHG. For this we initially assume a simple point emitter in vacuum which possesses an isotropic emission pattern and will focus on the forward-emitted hemisphere as is detectable in our set-up. Due to the isotropic nature of the point-emitter, no further weighting of any direction is necessary. The objective lens will collect all light emitted at angles at or smaller than its acceptance angle $\theta = asin(NA/n)$, governed by the numerical aperture NA and the environment refractive index n. We can therefore integrate over the intensity emitted into a cone with opening angle θ and divide the result by the total intensity emitted into the hemisphere, resulting in the collection ratio R_C plotted in Fig. 3 of the main document:

$$R_C = -[cos(\theta) - 1]. \tag{2}$$

However, the light generated during SHG is the result of radiation from the induced polarization caused by interaction of the incoming laser beam with the non-linear optical tensor of the sample. For congruent lithium niobate, this is calculated as:

$$\begin{pmatrix} P_x \\ P_y \\ P_z \end{pmatrix} = \begin{bmatrix} 0 & 0 & 0 & 0 & d_{15} & d_{16} \\ d_{21} & d_{22} & 0 & d_{24} & 0 & 0 \\ d_{31} & d_{32} & d_{33} & 0 & 0 & 0 \end{bmatrix} \begin{pmatrix} E_x^2(\omega_f) \\ E_y^2(\omega_f) \\ E_z^2(\omega_f) \\ 2E_y(\omega_f)E_z(\omega_f) \\ 2E_x(\omega_f)E_z(\omega_f) \\ 2E_x(\omega_f)E_y(\omega_f) \end{pmatrix} \tag{3}$$
$$= \begin{pmatrix} 2d_{15}E_xE_z + 2d_{16}E_xE_y \\ d_{21}E_x^2 + d_{22}E_y^2 + 2d_{24}E_yE_z \\ d_{31}E_x^2 + d_{32}E_y^2 + d_{33}E_z^2 \end{pmatrix}$$

In our present experiment, an x-polarized incidental beam was used. As has been previously shown by Amber et al.[2], the dominant polarization (and therefore the dominant emitting dipole) is orientated parallel to the crystallographic z-axis. For said dipole parallel to z, the emission pattern is proportional to $(1 - cos^2\theta_z)$, where θ_z is the angle with regards to the z-axis. Similar to the case of the point emitter, we can calculate the portion of light emitted into the forward hemisphere within a cone of opening angle θ. As our objective is located along the y-axis with respect to the dipole, we are interested in light emitted into cones of a given angle θ_y with respect to the y-axis. The previous $(1 - cos^2\theta_z)$ behavior becomes $cos^2\theta_z$ and is sketched in Fig. S3. As the angular distribution is symmetrical with regards to the y-axis, we are able to limit the integration boundaries from 0 to $\pi/2$ and must only double the result of the integration. However, as both the numerator and denominator contain the same factor, we can neglect it. The ratio R_C of collected light to total emitted light can thus be calculated as:

$$R_C = \frac{\int_0^{\theta_y} \cos^2\theta_y d\theta_y}{\int_0^{\pi/2} \cos^2\theta_y d\theta_y}. \tag{4}$$

The ratios for both a point emitter as well as dipole radiation in vacuum are presented in Fig. S4 as a function of the collection angle.

The above figure represents the ideal case in which the radiation occurs in an $\varepsilon = 1$ medium, i.e. vacuum. However, in the present experiment, the polarization is generated within the lithium niobate crystal and must then be refracted outside of the crystal according to Snell's law $n_{LN} \sin\alpha_{crystal} = \sin\alpha_{air}$, n_{LN} being the extraordinary refractive index of lithium niobate at the Second Harmonic frequency, here 450 nm. Additionally, there will be reflection at the boundary between the medium and air with the reflection being given by the Fresnel equations.

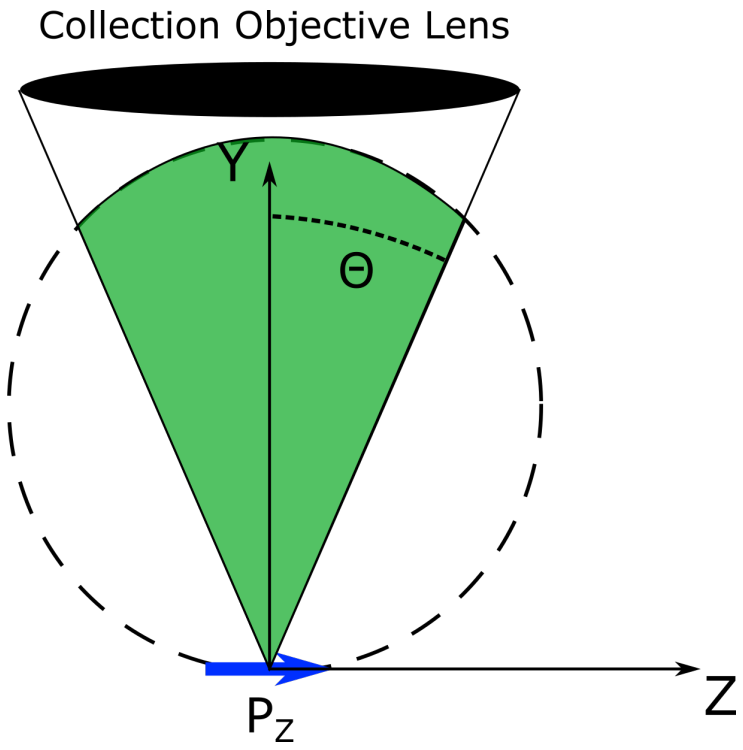

FIG. S3. Dipole radiation of a dipole aligned parallel to the z-axis is collected by a collection objective with an acceptance angle of θ located along the y-axis. The collected fraction of the emitted radiation is shaded in green

As we have a maximum collection NA of 0.55, we also have a maximum angle of emission within the crystal which we are still capable of collecting, which can be calculated from Snell's law for a 900 nm fundamental wavelength:

$$\sin \alpha_{max} = 0.55/2.2809 \rightarrow \alpha_{max} = 13.95^{\circ}. \tag{5}$$

It therefore makes sense to use the signal collected up to an angle of 13.95° as the normalization factor for future plots. Fig. S5 shows the collected signal from a dipole within an LN crystal with and without consideration of the Fresnel equations. For lower angles, the reflection coefficients only change by -0.00812 and $+0.00825$ for a 14°-incidence and is therefore relatively miniscule. Our maximum collection angle is only 13.95°, so we are still within the range in which this is the case. We can therefore safely disregard the slight change in reflectivity from a change in angle of incidence to the surface. From Fig. S5, we would expect a linear scaling of the collected signal with increasing NA.

We will now look at the ratio of the collected signal compared to the signal gathered at a numerical

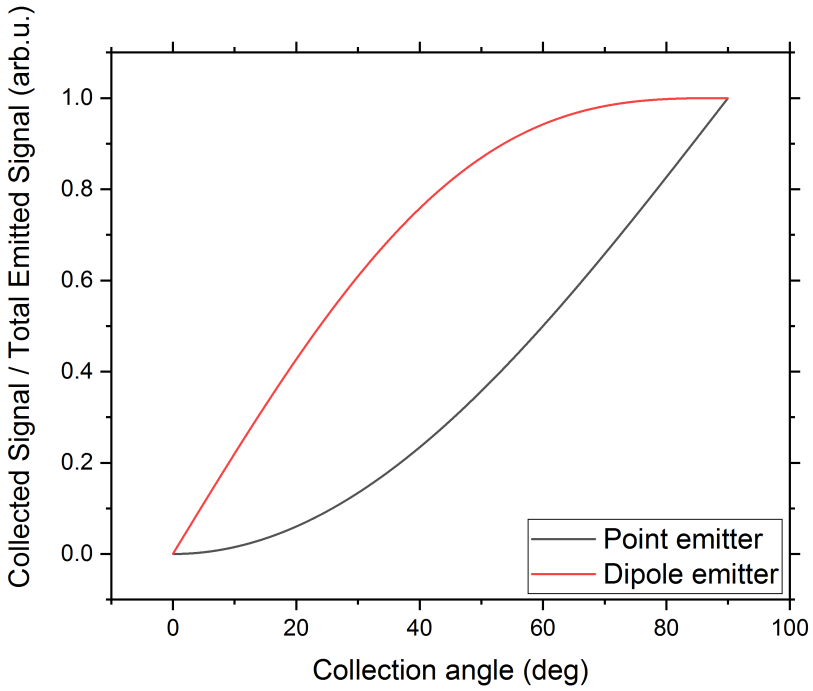

FIG. S4. Ratios of collected light to total emitted light for a point emitter (black) and a dipole (red), each in vacuum, for a given collection angle in air.

aperture of 0.55 for three different wavelengths in the congruent lithium niobate crystal. The wavelengths investigated are 900 nm, 950 nm and 1000 nm, with the ratios of the collected signal to the 0.55 NA signal presented in Fig. S6. These plots also include the theoretically expected behavior for both a dipole emitter within the LN crystal, as well as a point emitter in vacuum for the sake of direct comparison. Each wavelength was sampled in steps across the range in broader steps. Prior to this, we calculated the value of the numerical aperture at which we expect to see a change in the collected signal due to the sudden absence of CSHG light. The theoretically expected transition points are presented in Tab. S1. Around these expected numerical apertures, a finer graduation of 0.01 was chosen.

We can see that the surface signal behaves close to like we would expect for a dipole located within the lithium niobate crystal. That is, we see a more or less linear increase with increasing NA to begin with, although there is a slightly slower rate of change towards our maximum NA. This behavior also seems unaffected by the wavelength with which we investigate the sample. For all three wavelengths, however, the domain wall signal shows an obvious deviation both from

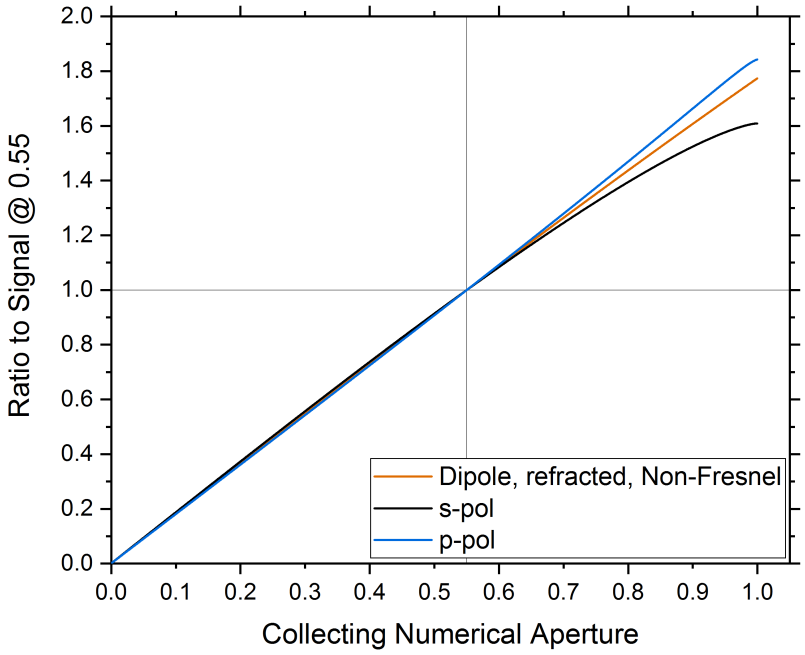

FIG. S5. Ratio of the signal at a given NA normalized to the signal at an NA of 0.55. The dipole is positioned within the lithium niobate crystal and the emitted light is refracted off the crystal-air boundary. The ratio disregarding any influence of the change in reflectance according to the Fresnel equations is shown in brown. The black and blue curves show the corresponding curves for s- and p-polarized light, respectively.

the surface signal as well as the expected behavior for the dipole. An initial slow increase is followed by a sharp change in the slope as soon as a certain threshold NA is reached.
Based on this we can assume that there is indeed some additional contribution to the real detected signal which is not present in the dipole-emission model and cannot be detected with a lower NA. The behavior of the signal, i.e. this unexpected contribution, can be best explained by CSHG.

In order to obtain an estimate on where the threshold NA for each wavelength lay, we calculated the discrete derivatives $D[i]$ of the data points, using the counts $S[i]$ as:

$$D[i] = \frac{S[i+1] - S[i]}{NA[i+1] - NA[i]}. \tag{6}$$

The switch point was then determined as the value of the NA at which the sudden increase in signal strength begins, as prior to the switch the derivative shows a roughly linear behavior. An estimate for the relative error of the calculated points was gained from the propagation of uncertainty for

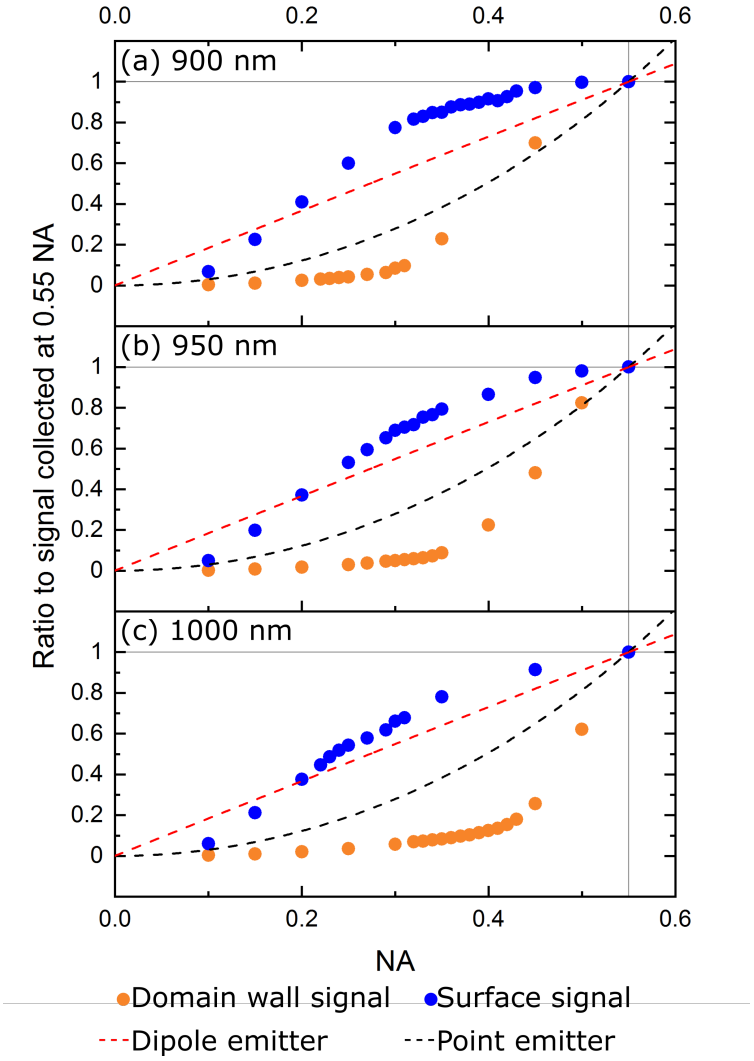

FIG. S6. Ratio of the signal for a given NA normalized to the signal collected using a numerical aperture of 0.55 for (a) 900 nm, (b) 950 nm, (c) 1000nm versus the corresponding collection NA. The plots include the theoretical behavior for a point emitter in vacuum and a dipole emitter within a lithium niobate crystal. The surface signal behaves close to what we would expect a dipole emitter to behave as for all three wavelengths. In contrast to this, the domain wall signals behave neither like a dipole nor like a point emitter, as is visible by the sudden sharp increase in signal contribution upon exceeding a certain threshold NA. It is important to note that the threshold NA decreases with an increase in wavelength.

the discrete derivative $D[i]$ resulting in Eq.(6), where we used a relative error of 1% of the signal

level and an NA error of 0.002:

$$\begin{aligned}(\Delta D[i]_{rel} \cdot D[i])^2 =& \left(\frac{1}{NA[i+1]-NA[i]}\right)^2 \cdot (0.01 \cdot S[i+1])^2 \\ &+ \left(\frac{1}{NA[i+1]-NA[i]}\right)^2 \cdot (0.01 \cdot S[i])^2 \\ &+ \left(\frac{S[i+1]-S[i]}{(NA[i+1]-NA[i])^2}\right)^2 \cdot (0.002)^2 \\ &+ \left(\frac{S[i+1]-S[i]}{(NA[i+1]-NA[i])^2}\right)^2 \cdot (0.002)^2.\end{aligned} \tag{7}$$

This relative error of the discrete derivative was then taken as the relative error of the measured threshold NA. The results are listed in Tab. S1 and plotted in Fig. S7 alongside the expected threshold NAs for the accessible wavelength range.

Wavelength	Threshold NA	Theory
900 nm	$0.41 \pm 30.1\%$	0.409
950 nm	$0.34 \pm 30.3\%$	0.325
1000 nm	$0.29 \pm 28.7\%$	0.240

TABLE S1. Threshold NA values calculated from the discrete derivatives of the signal level dependent on collection NA and the theoretically expected values. Calculated for 900 nm, 950 nm and 1000 nm.

We can see from Fig. S7 that the threshold NA does in fact decrease with higher wavelengths as predicted. As the errors included in Fig. S7 were based on the relative error of the discrete derivative calculated with a limited step size, the actual error may be slightly lower. However, due to the close match to the theoretical values, even without error bars, it seems very much likely that the behavior is due to CSHG emission within the crystal.

To summarize, based on the ratios of the collected signal to the maximum collected signal, we can show that the emission from the sample surface behaves as if it originates from a dipole placed shortly beneath the surface. On the other hand, the domain wall signal shows an additional contribution above a certain threshold NA, which causes a rapid increase in signal. This threshold also decreases for higher wavelengths, which would be expected from the smaller CSHG emission angles.

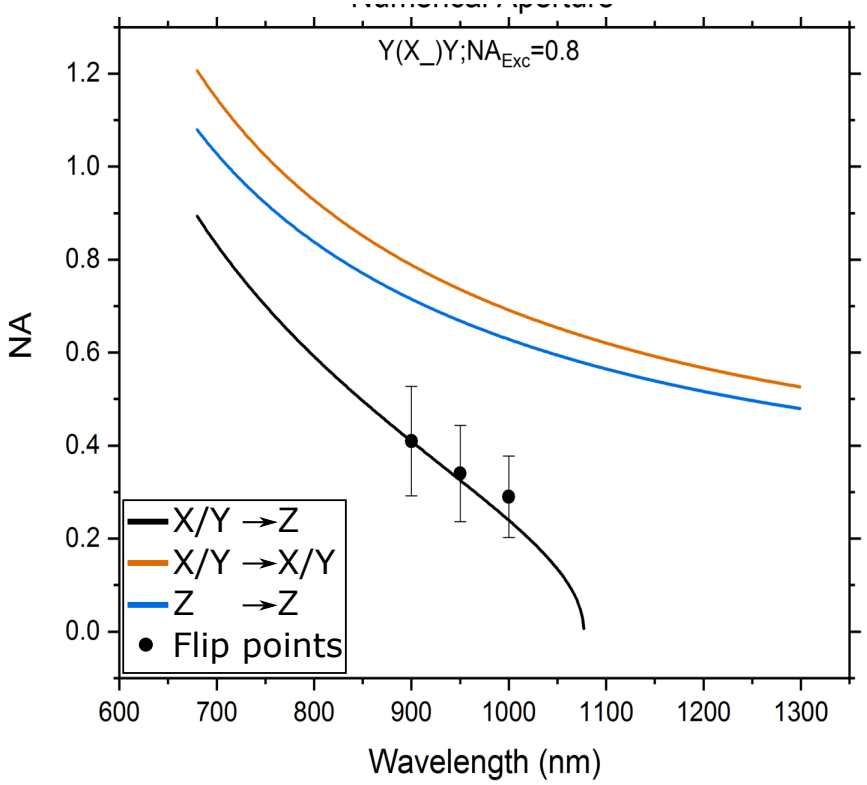

FIG. S7. Threshold NA values below which the system should no longer collect the signal emitted via CSHG. The curves represent calculated theoretical values. The experimental data points are the thresholds determined from the discrete derivative of the signal level for the chosen wavelengths.

S3. RESULTS WHEN VARYING THE COLLECTION NA

The previous section concerned itself with two obviously different situations in the form of the domain wall in the bulk and the surface of the domain region. It would now be of interest to investigate the region that is essentially the combination of the two, in other words domain walls at the surface of the crystal. As we have seen in the main text, we expect the domain wall to show as a bright line on the slightly darker surrounding domain for higher NAs, and eventually switch to appearing as a dark line on the brighter background of the surface. From the previous section we have already obtained an estimate for the threshold NA for our investigated sample, which we can use to focus on the relevant region around the flip point. Additionally, the base behavior of the system seems to be the same across the wavelengths, such that we can assume it is sufficient to only investigate one of the wavelengths. We will therefore limit the following section to the images recorded at 900 nm with its transition at an NA of ≈ 0.41 for now.

Fig. S8 shows the XY slices of the sample zoomed in to the surface for numerical apertures ranging from 0.33 to 0.43.

Above the threshold, we clearly discern the domain walls as brighter lines on the slightly less bright surface However, at the determined threshold NA of 0.41, the walls still show the same behavior instead of having flipped to the dark contrast. The first signs of a switch do not appear until 0.39 NA, when the domain walls seem to become slightly broader and a dark section appears in the middle. For further lowering of the collection NA, this dark line both lengthens and broadens, while the immediate surrounding area becomes slightly brighter compared to the domain region. At approximately 0.34 NA and lower, the domain wall signature at the surface seems to have fully converted to the negative contrast.

While the change in behavior for the domain walls deep within the material seemed to have been a relatively sudden process, the transition at the surface is instead gradual. Fig. S9 presents the line profiles for a select number of numerical apertures shown in Fig. S8 in order to gain a closer view.

As expected above the threshold NA, the domain walls show as positive peak signatures compared to the domain region. However, this behavior remains for an NA down to 0.39, lower than the threshold of 0.41. For lower NAs, we see the emergence of the dark line in the center of the domain wall as well as the slightly brighter strips immediately surrounding it. For numerical apertures below 0.33 we then only see the negative contrast of the domain wall on the domain region.

In order to offer a comparison, the profiles both 5 μm above the surface as well as 50 μm within the crystal are plotted in Figs. S10 and S11. In the former we can observe a similar transition to that in Fig. S9, as the obvious positive signatures of the domain wall decrease and subsequently disappear with lower NA. Generally, we observe a noticeable drop in domain wall signal compared to the surrounding domain, as is visible in Fig. S11 which is most likely simply owed to the lower collection range (compare Fig. S4).

As shown previously, both the surface domain region and the domain walls within the crystal each show a distinct behavior. It is possible that the transition in the behavior of the walls over a larger NA range at the surface is therefore the result of some interplay between the two. At this point we would also have the question of the bright border around the darker domain wall line. An initial thought would be akin to that proposed by Deng et al.[3] in that a certain roughness of the domain wall causes CSHG at a slight angular spread rather than collimated beams as assumed

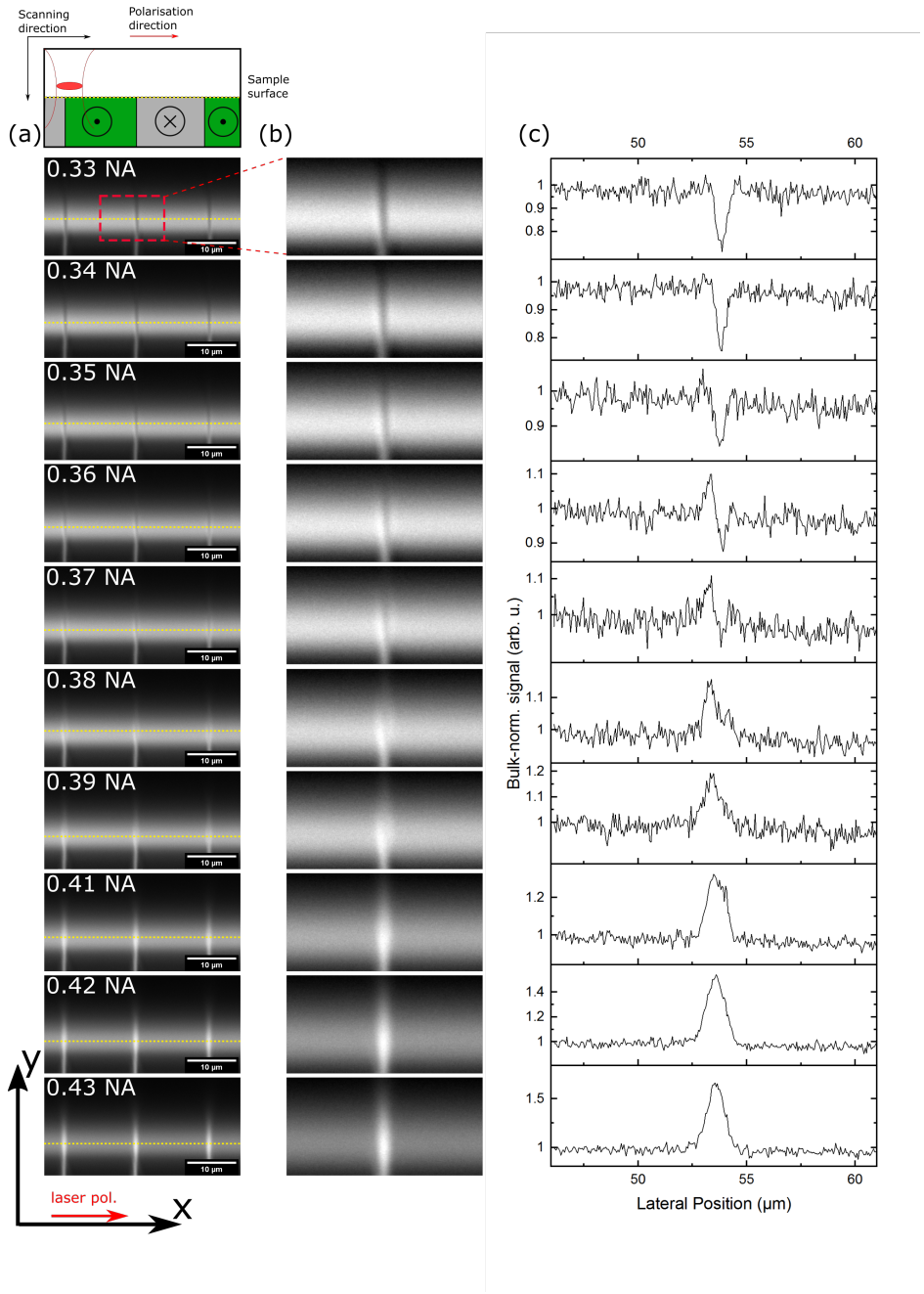

FIG. S8. Subfigure (a): XY cross-section of a y-cut cLN crystal polarized by an x-polarized beam incident along the crystal y-axis for a range of wavelengths around the threshold estimated in Fig. S7. We do see the transition from a bright line on darker background to a dark line, however, the transition seems to happen later than both expected and calculated in the previous section. Subfigure (b): Close-up of the domain wall outlined by the red-dashed box in subfigure (a). Subfigure (c): Normalized signal profile across the centre of the zoomed-in images in subfigure (b).

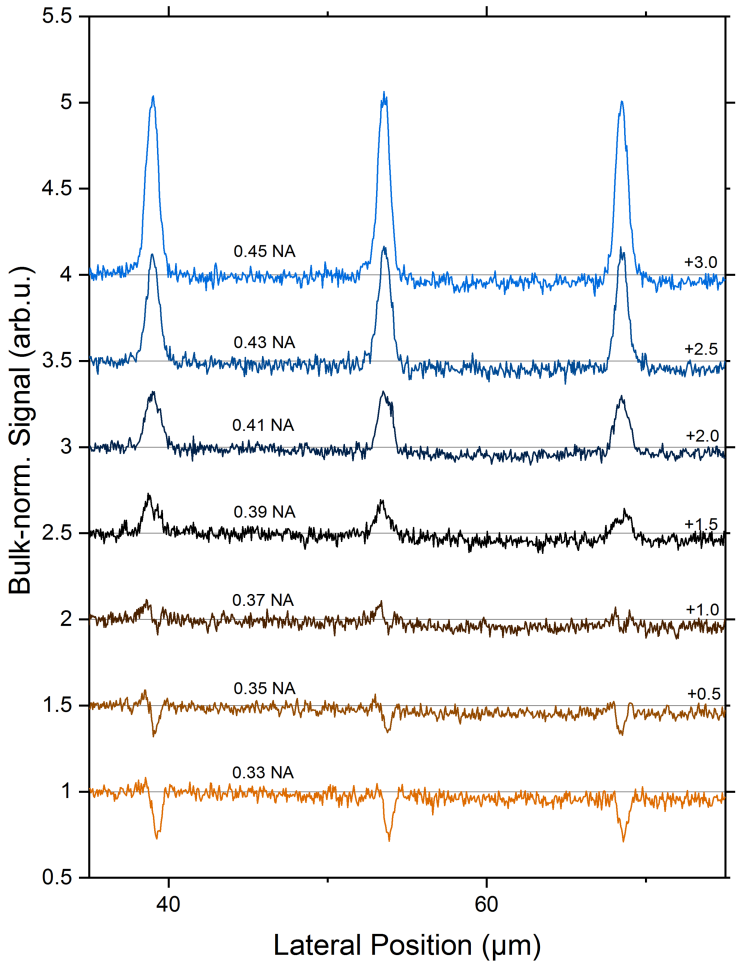

FIG. S9. Line profiles taken at the surface of a y-cut cLN crystal illuminated by an x-polarized beam incidental along the crystal y-axis using a focusing NA of 0.8 and fundamental wavelength of 900 nm. The profiles are normalized and offset to allow comparison. We see that domain walls in profiles above the expected threshold of 0.41 show the behavior we would expect of bright lines, however, this is also true down to 0.39 NA, lower than the expected threshold. 0.37 NA and lower seem to begin to show the dark line we would have expected, although there is a slight increase in the signal strength in the immediate surroundings. The profile taken using a collection NA of 0.33 NA is the last to show any noticeable signs of this increase that cannot simply be explained by a statistical deviation.

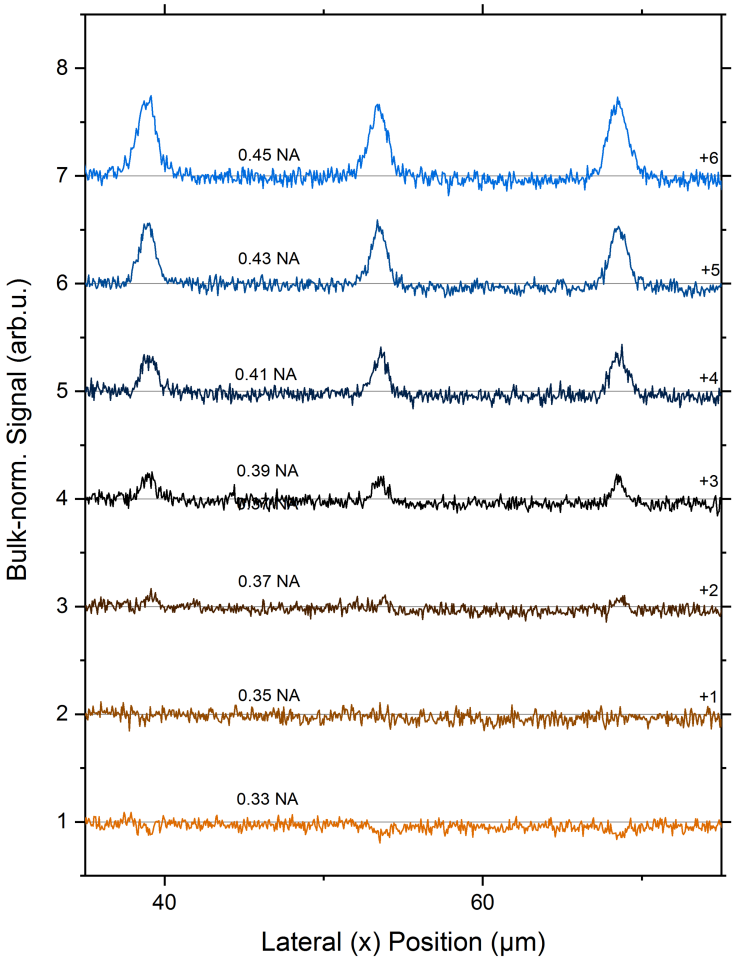

FIG. S10. Line profiles taken above the surface of a y-cut cLN crystal (sample 1) illuminated by an x-polarized beam incidental along the crystal y-axis using a focusing NA of 0.8 and at a fundamental wavelength of 900 nm. The profiles are normalized and offset to allow comparison. As with the profiles at the surface, higher collection numerical apertures display a more pronounced domain wall signature, which slowly disappears with lower NA.

in our calculated model. Due to the difference in acceptance angle between an NA of 0.41 and 0.35 being only $\Delta\alpha_O = \arcsin 0.41 - \arcsin 0.35 \approx 4^\circ$, a sufficiently rough wall could therefore scatter a limited amount of SH light into the objective. However, we would then expect the effect

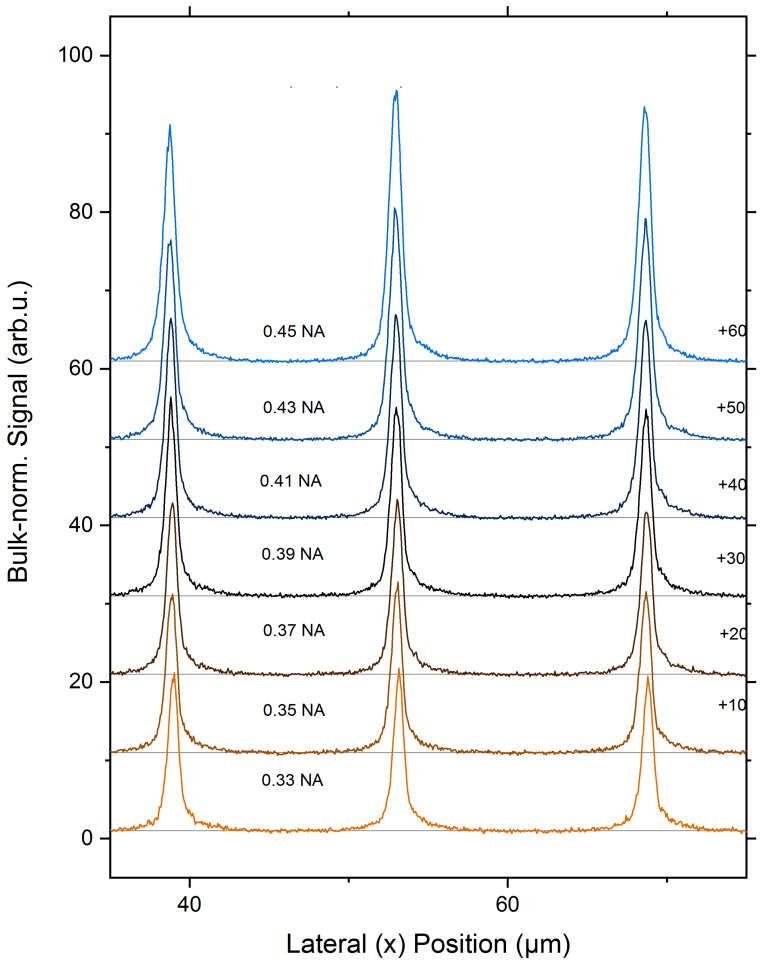

FIG. S11. Line profiles taken 50 μm below the surface of a y-cut cLN crystal illuminated by an x-polarized beam incidental along the crystal y-axis using a focusing NA of 0.8 and a fundamental wavelength of 900 nm. The profiles are normalized and offset to avoid cluttering. There is no significant change in the domain wall signature outside of the decrease in relative strength compared to the surrounding domain signal.

of which to be noticeable in the center of the domain wall, rather than immediately to either side, which would make a superposition of multiple co-existing mechanisms seem the most likely explanation.

S4. COMPARISON OF REGION STRENGTH

The region types assigned in Figs. 2(c) and 2(d) of the main text were based on two assumptions, one being the lateral displacement of CSHG beams which changes with wavelength and causes the formation of the type-II and type-III regions, the other assuming that within the type-I region both emitted CSHG beams simply overlap linearly instead of interacting non-linearly. This was verified by extracting the profiles from Fig. 4(e) in increments of 50 μm in order to compare the magnitude of the DW signature peaks. An overlay of the profile extracted from a depth of 500 μm and from 900 μm is depicted in Fig. S12. Each profile contains only contributions from a type-II or type-I region, respectively. However, a straight comparison is difficult, as the signal strength decreases with increasing depth within the crystal, for example due to dissipation or absorption effects. In order to calculate the CSHG signal strength within a single type-II region, a linear fit was made using the magnitudes of the DW signatures for depths from 100 μm to 800 μm and is shown in Fig. S13. This linear equation was then used to calculate the theoretical type-II CSHG signal at a depth of 900 μm and the resulting value was compared to the type-I signal strength extracted from Fig. 4(e) at 900 μm.

The values for each respective signal strength were determined as 16689,89 arb.u. for the theoretical type-II region at a depth of 900 nm, and 37545 arb.u. for the type-I region visible in Figs. 4(d)-4(f) (main text). By comparing these two values, we see that the DW signatures in the type-I region is roughly twice as strong as would be expected from a type-II region at the given depth. This indicates that the signal a type-I region is indeed simply the linear superposition of that of two type-II regions.

Signal source	Type-II	Type-I
Signal value (arb. u.)	16689,89	37545

TABLE S2. Theoretical single CSHG signal compared to the signal from the type-I region in Fig. 4(e).

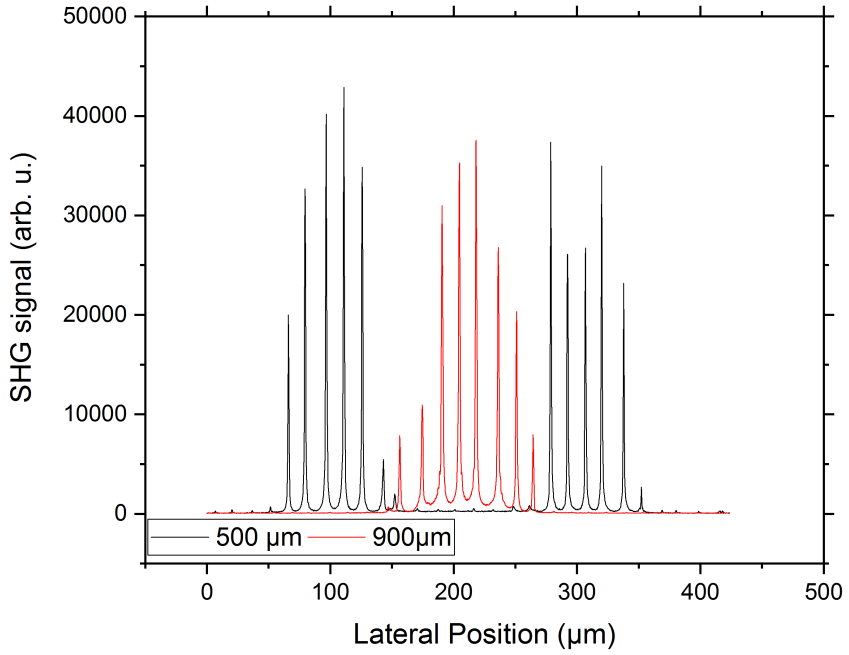

FIG. S12. Signal profiles extracted from Fig. 4(e) at a depth of 500 μm (black) and 900 μm (red), representative of a type-II and type-I region, respectively.

S5. OBTAINING THE EMISSION ANGLES

The images shown in Fig. 4(d) through 4(f) in the main text were used to calculate the angle between the border of the type-II regions and the vertical axis, i.e. the CSHG emission angle within the crystal. As the signal generated from DWs fluctuates with any kinks or irregularities within the DW itself, an accurate location of the border between the type-II and type-III regions proves difficult. Instead, each image was transformed into a number of binary representations as shown in Fig. S14 for the case of Fig. 4(e), by selecting a set minimum and maximum display value that are only seperated by 1, i.e. 3000 and 3001 as the minimum and maximum, respectively. This effectively acts as a binning threshold and results in the above images for thresholds of (a) 3000; (b) 5000; (c) 7000, and (d) 10000 counts.

These binary images deliver a sharp transition between the two types of regions and allow us to accurately locate the border. The positions within the image were subsequently transformed into the actual crystal positions and plotted as shown in Fig. S15. Each side of the image, and therefore each border between a type-II and type-III region, was treated separately and approximated with

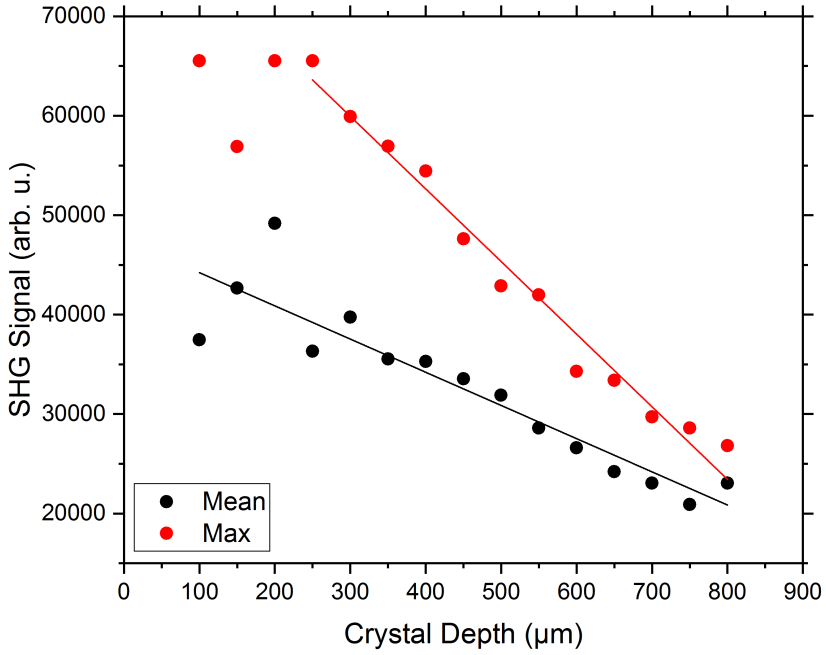

FIG. S13. Maximum and mean DW signature magnitudes from the type-II region in Fig. 4(e), plotted versus their respective depth within the crystal. A linear fit was performed while excluding the first three data points due to overexposure of the detector and therefore an artificial limit to the signal strength.

a linear fit of the determined positions. As stated in the main text, the slope A of the linear fits correlates to the inclination angle with respect to the vertical axis α, as $\alpha = arctan(1/A)$.

S6. CALCULATING EXPECTED SURFACE PROFILES

In order to obtain an initial estimate of the relative strength of CSHG compared to the surface-emitted SHG usually seen with the investigated samples, it is necessary to identify the signal profile we would expect from a pure surface emission when utilizing the bright-field aperture. As detailed in the first section of this supplement, the emission pattern of the surface follows a $[1 - cos^2(\theta)]$-behavior, where θ is the angle between the polarization and emission direction. As our dipole at the surface is oriented along the z-axis and the aperture is located along the y-axis from the surface, we can therefore treat the emission pattern as $cos^2(\theta_y)$, with θ_y being the angle with respect to the y- (or vertical) axis.

The front surface was then discretized into an array of x-positions. From each position X_p, the

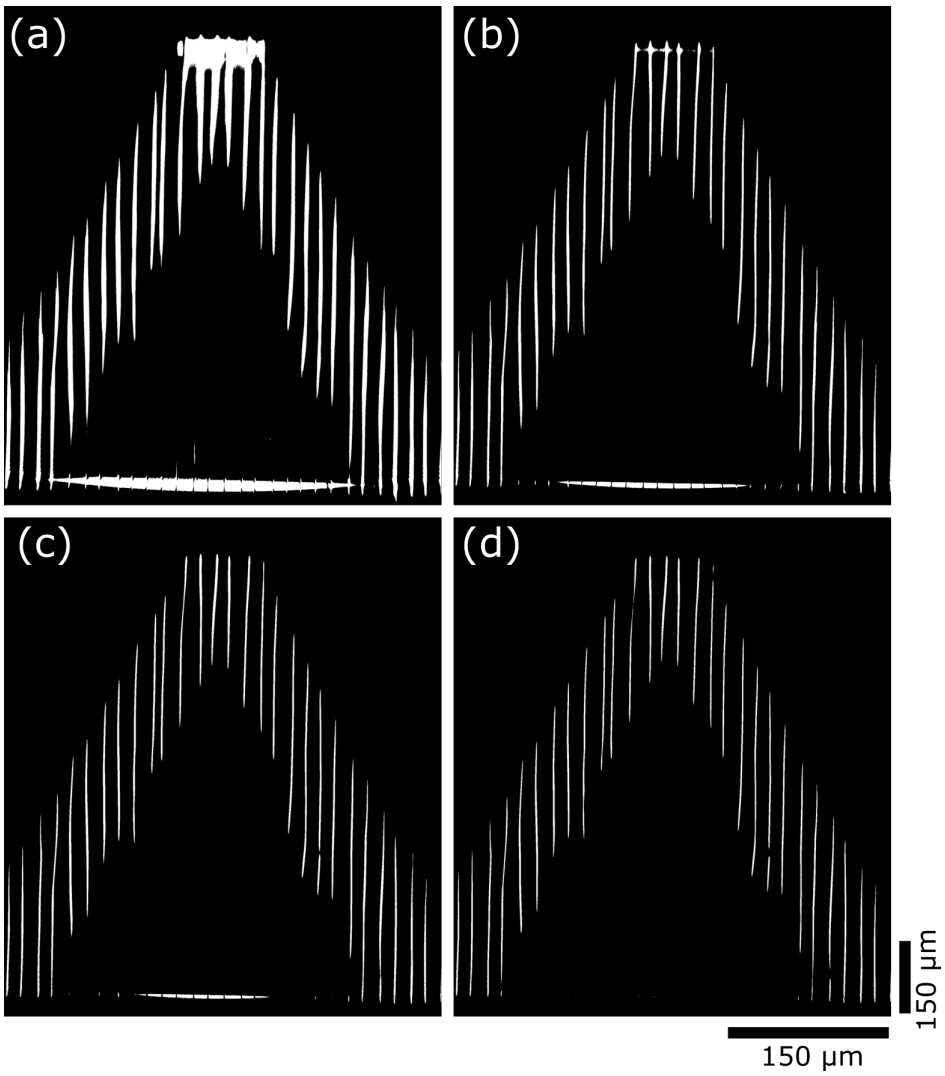

FIG. S14. Binary transformations of Fig. 4(e) in the main text generated by choosing a set threshold level to perform binning. The respective thresholds are (a) 3000, (b) 5000, (c) 7000 and (d) 10000 counts, respectively.

angle from said point to both the left and right edge of the aperture opening was calculated, as only light emitted at an angle between these two from the point X_P will be able to exit the aperture. These angles were calculated as $\alpha_L = arctan[(X_L - X_P)/h]$, with h the (optical) thickness of the crystal. The angle to the right edge α_R was calculated analogously.

For simplicity's sake, the radius of the emission pattern was set to 1 during integration. As we are only interested in the qualitative trend of the signal profile, we also neglect the normalization to the total emitted intensity. The signal emitted into the aperture opening for a given point X_P is

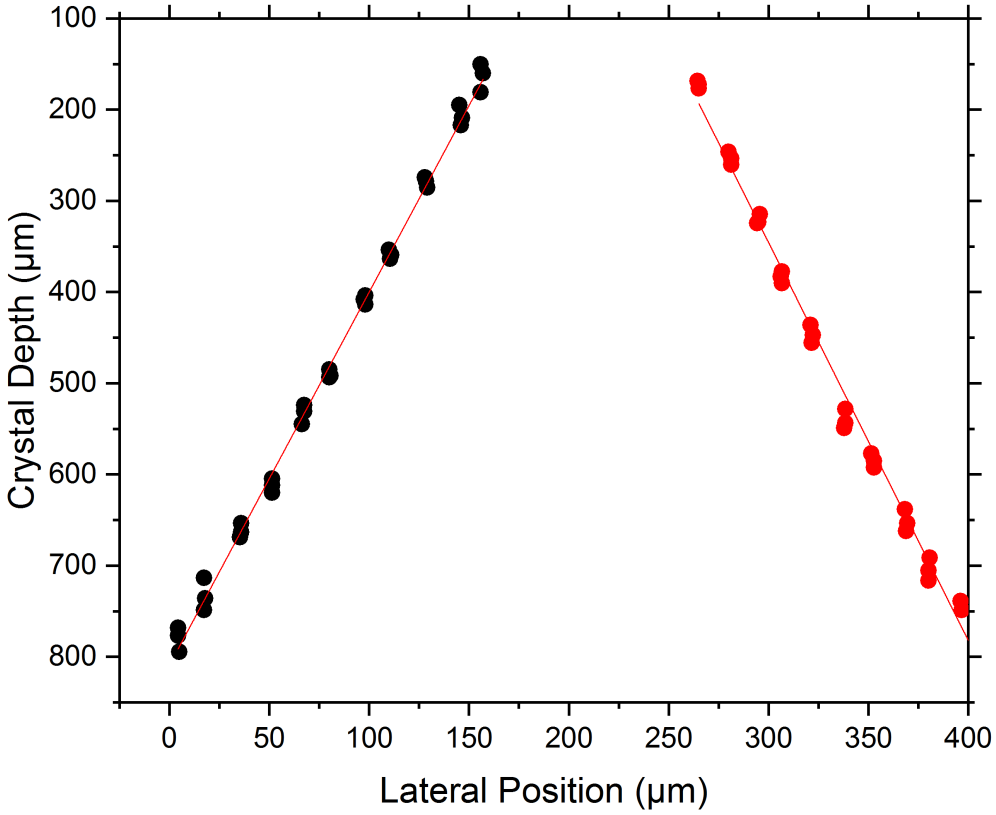

FIG. S15. Crystal positions of the border between the type-II and type-III regions in Fig. S14. Each side of the triangular region within the image was treated separately and was used to perform a linear fit in order to approximate the actual border. The slope of each fit was then used to calculate the emission angle with respect to the vertical as described in the main text.

then calculated as

$$\int_{\alpha_L}^{\alpha_R} cos^2(\alpha')d\alpha'. \tag{8}$$

The calculated curve was then re-normalized to the signal level measured in Fig. 4(e) and added to Fig. 6 (main text) as the expected theoretical signal profile. We can therefore see that the parabolic shape of the profile is solely a result of the surface-dipole emission through the aperture opening and not any effect of the collected or blocked CSHG.

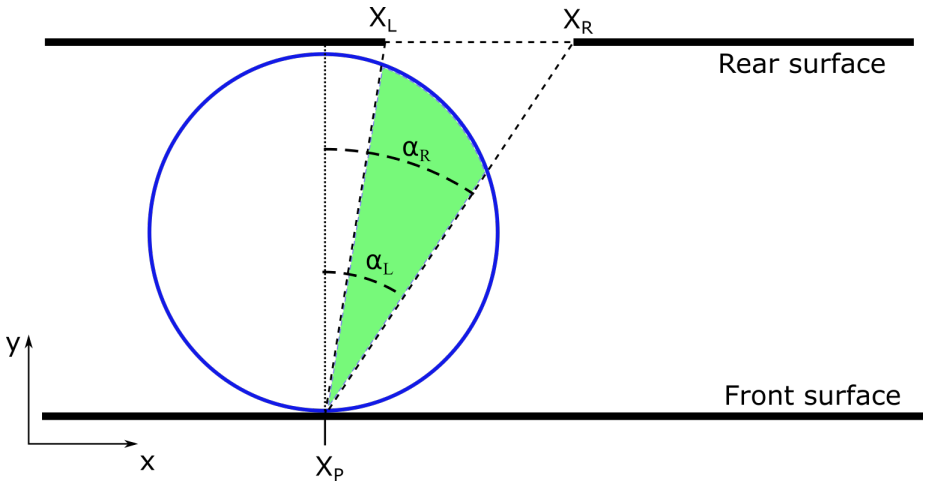

FIG. S16. Sketch of the parameters used to calculate the expected signal profile emitted at the surface for a measurement recorded with a bright-field aperture. The green-shaded area originating from X_P is the fraction of the signal that will exit the aperture opening between X_L and X_R.

REFERENCES

[1]S. Hell, G. Reiner, C. Cremer, and E. H. Stelzer, "Aberrations in confocal fluorescence microscopy induced by mismatches in refractive index," J. Microscopy **169**, 391 (1993).

[2]Z. Amber, B. Kirbus, L. Eng, and M. Rüsing, "Quantifying the coherent interaction length of second-harmonic microscopy in lithium niobate confined nanostructures," J. Appl. Phys. **130**, 133102 (2021).

[3]X. Deng and X. Chen, "Domain wall characterization in ferroelectrics by using localized nonlinearities," Opt. Express **18**, 15597 (2010).